A molecular dynamics approach to magnetic alloys with turbulent complex magnetic structures: γ-FeMn alloys

1998 J. Phys.: Condens. Matter 10 2081

(http://iopscience.iop.org/0953-8984/10/9/013)

J. Phys.: Condens. Matter **10** (1998) 2081–2105. Printed in the UK PII: S0953-8984(98)88599-8

A molecular dynamics approach to magnetic alloys with turbulent complex magnetic structures: γ-FeMn alloys

S Akbar, Y Kakehashi and N Kimura
Hokkaido Institute of Technology, Maeda, Teine-ku, Sapporo 006, Japan

Received 21 October 1997

Abstract. A molecular dynamics (MD) approach to magnetic alloys with complex magnetic structures is proposed on the basis of the temperature control MD method and the functional integral technique. The theory allows us to determine automatically the magnetic structure of a large system with a few hundred atoms in a unit cell. Numerical calculations for γ-FeMn alloys have been performed using 108 atoms in a unit cell. It is demonstrated that γ-FeMn alloys form various complex magnetic structures due to competing interactions: the 'first-kind' antiferromagnetic structure for less than 20 at.% Fe, the helix-like structure for 20 at.% Fe, noncollinear structures between 30 and 60 at.% Fe, the collinear-like structure for 65 at.% Fe, noncollinear structures between 70 and 80 at.% Fe, collinear structures between 85 and 95 at.% Fe, and the helical structure for γ-Fe. The average magnetic moments calculated from these structures are shown to explain the concentration dependence—in particular, the existence of the peculiar minimum of the average magnetic moment at 50 at.% Fe.

1. Introduction

In the last half century, a large number of investigations have been carried out, and notable progress in the theory has been made as regards the electronic structure and magnetic properties of 3d transition metals and alloys. For example, the development of first-principles theories enabled us to calculate quantitatively the ground-state magnetization of Fe, Co, Ni, and their compounds [1]. The coherent potential approximation (CPA) theory [2] explained the basic aspects of the Slater–Pauling curves for the ferromagnetic 3d transition metal alloys [3]. Recent finite-temperature theories [4–8] using the CPA clarified the magnetic properties of transition metals and alloys at finite temperatures.

Very little progress in the theory, on the other hand, has been achieved as regards achieving an understanding of the magnetic structures and properties of 3d elements and their alloys with nearly half-filled bands such as Cr, Mn, γ-Fe, and their alloys, since they show complexity in the magnetic structures and anomalies due to competing interactions.

The investigations using the band theories to explain the complex magnetic structures have been based on a simple energy comparison among several possible magnetic structures, or the minimization of the free energy with respect to the order parameters found from experiments, or susceptibility analysis for the magnetic instability against fluctuations around the nonmagnetic state. Although they are useful for finding the electronic origin of the stability of the magnetic structures, they are not suitable for determining complex magnetic structures, since these methods do not guarantee global minima of the systems. This is a serious drawback for the systems in which there are many local minima in the free energy due to competing interactions. We therefore recently developed a molecular dynamics method

0953-8984/98/092081+25$19.50

for itinerant-electron systems with competing magnetic interactions [9] on the basis of the functional integral method [4–8, 10] and the MD method [11, 12]. The theory allows us to determine automatically the global minimum of the free energy in the systems with large unit cells, and hence the complex magnetic structure of the systems. Moreover, it describes the second-order phase transition with increasing temperature due to the self-consistent determination of the effective medium.

We have demonstrated in our previous paper [9] the existence of a variety of complex magnetic structures in the fcc transition metals with d-electron numbers in the range between 6.0 and 7.0, where the ferromagnetic and antiferromagnetic interactions are expected to compete with each other. We obtained the 'first-kind' antiferromagnetic (AFI) structure for γ-Mn with a magnetic moment $2.5\mu_B$, and the helical spin structure for γ-Fe with a magnetic moment $0.75\mu_B$ and the wave vector $\boldsymbol{Q} = (0, 1/3, 2/3)\,2\pi/a$ using 108 atoms in a unit cell; these results are consistent with those from experiments although the wave vector is somewhat different from the experimental one: $\boldsymbol{Q} = (0, 0.1, 1)\,2\pi/a$ [13]. (Here a is a lattice parameter.) The rigid-band calculations of the average magnetic moment explained the concentration dependence in disordered γ-FeMn alloys up to 50 at.% Fe, but failed to explain the peculiar minimum at 50 at.% Fe and the behaviours beyond it. This suggests that extension of the theory to the disordered magnetic alloys is essential, even for a qualitative explanation of the magnetic properties.

In this paper, we extend our MD approach to the random magnetic alloys, and apply the theory to the disordered γ-FeMn alloys. The γ-FeMn alloys are well known to show complex magnetic structures in the concentrated region due to competing magnetic interactions and random atomic configuration. Neutron experiments [14] led to reports that there are three different types of spin structure for the alloys: (1) the γ-Mn type for concentration up to 30 at.% Fe; (2) the noncollinear spin arrangement for the concentration range between 35 and 75 at.% Fe; and (3) the γ-Fe type beyond 80 at.% Fe. In particular, a noncollinear structure called a multiple-spin-density wave with the three wave vectors $\boldsymbol{Q} = (1, 0, 0)\,2\pi/a$, $(0, 1, 0)\,2\pi/a$, and $(0, 0, 1)\,2\pi/a$ was proposed to exist at around 50 at.% Fe [14, 15], while collinear magnetic structure was reported for a single crystal of γ-$Fe_{66}Mn_{34}$ alloy in inelastic neutron scattering experiments [16, 17].

The first theoretical investigation for γ-FeMn alloys was carried out by Asano and Yamashita [18]. They explained the monotonic decrease of the average magnetic moment up to 50 at.% Fe within a rigid-band calculation assuming AFI structure, and obtained the density of states (DOS) of γ-Mn showing bonding and antibonding due to local exchange splitting as well as the DOS having the gap-like dip near the Fermi level for γ-$Fe_{50}Mn_{50}$ alloy. The rigid-band calculation, however, did not explain the minimum of the average magnetic moment at 50 at.% Fe and the rapid increase of the moment beyond 50 at.% Fe. Kübler *et al* [19] and Fujii *et al* [20] have performed total-energy band calculations for γ-$Fe_{50}Mn_{50}$ alloys assuming the CuAu-type crystal structure and a few possible noncollinear magnetic structures, but their calculations did not yield the three-$\boldsymbol{Q}$ spin-density wave proposed on the basis of the experiments. Süss and Krey [21] made calculations for the ordered γ-FeMn alloys with the collinear spin structure. They failed to obtain convergence in their self-consistent equations, and therefore also failed to obtain the magnetic structure.

The MD approach can determine the most stable structure among all of the possible magnetic structures in a large unit cell at finite temperatures. Therefore, the present approach possesses more possibilities for detailed investigations of magnetic structures in γ-FeMn alloys than the previous calculations. In particular, the approach to the substitutional alloys is more reliable as compared with that to the pure metals even if the size of the MD unit cell is not large, since the random potentials cause damping of long-range magnetic interactions

and the random atomic configuration generally suppresses the spin frustrations.

The organization of this paper is as follows. We formulate the theory in section 2. We derive in subsection 2.1 the free energy and related thermodynamic quantities on the basis of the functional integral method. Locally rotated coordinates will be introduced so that the free energy reduces to the generalized Hartree–Fock approximation at the ground state, which is suitable for the description of the noncollinear magnetic structures. In subsection 2.2, we present the molecular dynamics method for the random magnetic alloys, and the method of electronic structure calculations for the magnetic force. In section 3, we present the results of the numerical calculations for the magnetic structures and magnetic moments of γ-FeMn alloys. Various noncollinear structures are found beyond 20 at.% Fe. An interpretation of the stability of the structures is given on the basis of the calculated DOS. The results of calculations of the average magnetic moment are shown to explain the experimental data well except those for a narrow region around 70 at.% of Fe. A summary of this paper is given in the last section.

2. Formulation

2.1. The functional integral method

We adopt the following tight-binding d-band Hamiltonian with intra-atomic Coulomb interactions describing the magnetism in transition metal alloys:

$$H = H_0 + H_1 \tag{1}$$

$$H_0 = \sum_{i\nu\sigma} \epsilon_i^0 n_{i\nu\sigma} + \sum_{i\nu j\nu'\sigma} t_{i\nu j\nu'} a^\dagger_{i\nu\sigma} a_{j\nu'\sigma} \tag{2}$$

$$H_1 = \frac{1}{4}\sum_i U_i n_i^2 - \sum_i J_i \boldsymbol{S}_i^2. \tag{3}$$

Here ϵ_i^0 and $t_{i\nu j\nu'}$ are the atomic level at site i and the transfer integral for the orbitals ν at site i and ν' at site j, respectively. U_i (J_i) denotes the intra-atomic Coulomb (exchange) integral at site i. $n_{i\nu\sigma} = a^\dagger_{i\nu\sigma} a_{i\nu\sigma}$ is the number operator for the electrons at site i, with orbital ν and spin σ, and $a^\dagger_{i\nu\sigma}$ ($a_{i\nu\sigma}$) is the creation (annihilation) operator for an electron with spin σ and orbital ν at site i. n_i and $\boldsymbol{S}_i$ in the interaction part H_1 denote the charge and spin densities at site i, which are defined by $n_i = \sum_{\nu\sigma} n_{i\nu\sigma}$ and $\boldsymbol{S}_i = \sum_{\nu\sigma\sigma'} a^\dagger_{i\nu\sigma}(\boldsymbol{\sigma})_{\sigma\sigma'} a_{i\nu\sigma'}/2$, respectively.

To derive an expression for the free energy from the partition function which reduces to the generalized Hartree–Fock approximation at the ground state, we introduce locally rotated coordinates at each site, and rewrite the interaction Hamiltonian by means of operators $\{\hat{n}_{i\nu}, \hat{m}_{i\nu\alpha}\}$ on the rotated coordinates as follows:

$$H_1 = \frac{1}{8}\sum_{i\nu}(U_i + 3J_i)\hat{n}_{i\nu}^2 + \frac{1}{4}\sum_i U_i {\sum_{\nu\nu'}}' \hat{n}_{i\nu}\hat{n}_{i\nu'} - \frac{1}{8}\sum_{i\nu}(U_i + 3J_i)\hat{m}_{i\nu z}^2 - \frac{1}{4}\sum_i J_i {\sum_{\nu\nu'}}' \sum_\alpha \hat{m}_{i\nu\alpha}\hat{m}_{i\nu'\alpha}. \tag{4}$$

Here $\hat{n}_{i\nu} = \sum_\sigma \hat{a}^\dagger_{i\nu\sigma}\hat{a}_{i\nu\sigma}$ and $\hat{m}_{i\nu\alpha} = \sum_{\sigma\sigma'} \hat{a}^\dagger_{i\nu\sigma}(\sigma_\alpha)_{\sigma\sigma'}\hat{a}_{i\nu\sigma'}$. The creation ($\hat{a}^\dagger_{i\nu\sigma}$) and annihilation ($\hat{a}_{i\nu\sigma}$) operators for an electron with spin σ are quantized along the z-axis of the rotated coordinates at site i, and are given by

$$\hat{a}^\dagger_{i\nu\sigma} = \sum_{\sigma'} a^\dagger_{i\nu\sigma'} D_{\sigma'\sigma}(R_i) \tag{5}$$

$$\hat{a}_{i\nu\sigma} = \sum_{\sigma'} a_{i\nu\sigma'} D^{*}_{\sigma\sigma'}(R_i) \tag{6}$$

where $D_{\sigma\sigma'}(R_i)$ denotes a rotation matrix for a spin at site i.

The functional integral method provides us with an approximate calculation scheme for the partition function describing the spin fluctuations at finite temperatures. We apply the method to the Hamiltonian in terms of the rotated coordinates. The method transforms the interacting Hamiltonian into the one-electron Hamiltonian with time-dependent random charge and exchange fields $\{\zeta_{i\nu}(\tau), \boldsymbol{\xi}_{i\nu}(\tau)\}$ by adopting the Hubbard–Stratonovich transformation [22, 23]:

$$\begin{aligned} \mathrm{e}^{-\beta H_1(\tau)\Delta\tau} = {} & \left[\prod_{i=1}^{N}\left(\frac{(\Delta\tau)^D}{(4\pi)^D}\det A_i\right)^{1/2}\prod_{\alpha}^{x,y,z}\left(\frac{(\Delta\tau)^D}{(4\pi)^D}\det B_i^{\alpha}\right)^{1/2}\right]\int\left[\prod_{i=1}^{N}\prod_{\nu=1}^{D}\mathrm{d}\boldsymbol{\xi}_{i\nu}(\tau)\ \mathrm{d}\zeta_{i\nu}(\tau)\right] \\ & \times \exp\left[-\frac{\Delta\tau}{4}\sum_{i\nu\nu'}\left(\zeta_{i\nu}(\tau)A_{i\nu\nu'}\zeta_{i\nu'}(\tau) + \sum_{\alpha}\xi_{i\nu\alpha}(\tau)B^{\alpha}_{i\nu\nu'}\xi_{i\nu'\alpha}(\tau)\right)\right. \\ & \left. + \frac{\Delta\tau}{2}\sum_{i\nu\nu'}\left(\mathrm{i}\zeta_{i\nu}(\tau)A_{i\nu\nu'}\hat{n}_{i\nu'}(\tau) + \sum_{\alpha}\xi_{i\nu\alpha}(\tau)B^{\alpha}_{i\nu\nu'}\hat{m}_{i\nu'\alpha}(\tau)\right)\right] \end{aligned} \tag{7}$$

$$A_{i\nu\nu'} = \frac{1}{2}(U_i + 3J_i)\delta_{\nu\nu'} + U_i(1-\delta_{\nu\nu'}) \tag{8}$$

$$B^{\alpha}_{i\nu\nu'} = J_i(1-\delta_{\nu\nu'}) \qquad (\alpha = x, y) \tag{9}$$

$$B^{z}_{i\nu\nu'} = \frac{1}{2}(U_i + 3J_i)\delta_{\nu\nu'} + J_i(1-\delta_{\nu\nu'}). \tag{10}$$

Here β is the inverse temperature defined by T^{-1}. $H_1(\tau)$ denotes the Hamiltonian H_1 in the interaction representation and $\Delta\tau$ is an infinitesimal time interval. N (D) denotes the number of sites (orbital degeneracy), and $\det A_i$ denotes the determinant of matrix $A_{i\nu\nu'}$ for orbital indices.

The partition function is then written as

$$\begin{aligned} Z = {} & \int\left[\prod_{i=1}^{N}\prod_{\nu=1}^{D}\delta\boldsymbol{\xi}_{i\nu}(\tau)\,\delta\zeta_{i\nu}(\tau)\right]Z^0(\boldsymbol{\xi}(\tau),\zeta(\tau)) \\ & \times \exp\left[-\frac{1}{4}\sum_{i\nu\nu'}\int_0^{\beta}\mathrm{d}\tau\ \left(\zeta_{i\nu}(\tau)A_{i\nu\nu'}\zeta_{i\nu'}(\tau) + \sum_{\alpha}\xi_{i\nu\alpha}(\tau)B^{\alpha}_{i\nu\nu'}\xi_{i\nu'\alpha}(\tau)\right)\right] \end{aligned} \tag{11}$$

$$Z^0(\boldsymbol{\xi}(\tau),\zeta(\tau)) = \mathrm{Tr}\left[\mathcal{T}\exp\left(-\int_0^{\beta}H(\tau,\boldsymbol{\xi}(\tau),\zeta(\tau))\ \mathrm{d}\tau\right)\right] \tag{12}$$

$$H(\tau,\boldsymbol{\xi}(\tau),\zeta(\tau)) = K_0(\tau) - \frac{1}{2}\sum_{i\nu\nu'}\left(\mathrm{i}\zeta_{i\nu}(\tau)A_{i\nu\nu'}\hat{n}_{i\nu'}(\tau) + \sum_{\alpha}\xi_{i\nu\alpha}(\tau)B^{\alpha}_{i\nu\nu'}\hat{m}_{i\nu'\alpha}(\tau)\right). \tag{13}$$

Here $\mathcal{T}$ in equation (12) denotes the time order product. The operator K_0 in equation (13) is defined by $H_0 - \mu N_e$, μ and N_e being the chemical potential and the total number of electrons, respectively. The functional integral $\int[\prod_{\nu=1}^{D}\delta\zeta_{i\nu}(\tau)]$ in equation (11) is defined as

$$\int\prod_{n=1}^{N'}\left[\left(\frac{(\Delta\tau)^D\det A_i}{(4\pi)^D}\right)^{1/2}\prod_{\nu=1}^{D}\mathrm{d}\zeta_{i\nu}(\tau_n)\right] \to \int\left[\prod_{\nu=1}^{D}\delta\zeta_{i\nu}(\tau)\right] \tag{14}$$

where the imaginary time τ is divided into N' points in the range $[0, \beta]$, and τ_n stands for the nth point.

The functional integral method describes the basic behaviours of the spin fluctuations in the limits of strong and weak Coulomb interaction within the static approximation [7] which neglects the time dependence of the fictitious fields. By neglecting the transverse static spin fluctuations in the rotated coordinates, we can express the partition function in the static approximation as integrals over spatially fluctuating fields $\{\zeta_i, \xi_i\}$, which are conjugate to the charge-density operator $\hat{n}_i$ and spin-density operator $\hat{S}_{iz}$:

$$Z(\{\boldsymbol{e}_i\}) = \int \prod_{i=1}^{N} \left[\left(\frac{\beta \tilde{J}_i}{4\pi} \right)^{1/2} \mathrm{d}\xi_i \left(\frac{\beta \tilde{U}_i}{4\pi} \right)^{1/2} \mathrm{d}\zeta_i \right] \mathrm{Tr}(\mathrm{e}^{-\beta H_{\mathrm{st}}(\xi \boldsymbol{e}, -\mathrm{i}\zeta)}) \times \exp\left[-\frac{1}{4}\beta \sum_i (\tilde{U}_i \zeta_i^2 + \tilde{J}_i \xi_i^2) \right] \tag{15}$$

$$H_{\mathrm{st}}(\xi \boldsymbol{e}, \zeta) = \sum_{i\nu\sigma} \left(\epsilon_i^0 - \mu + \frac{1}{2}\tilde{U}_i \zeta_i \right) n_{i\nu\sigma} - \frac{1}{2} \sum_{i\nu} \tilde{J}_i \xi_i \boldsymbol{e}_i \cdot \boldsymbol{m}_i + \sum_{i\nu j\nu'\sigma} t_{i\nu j\nu'} a^{\dagger}_{i\nu\sigma} a_{j\nu'\sigma}. \tag{16}$$

The field variables ζ_i and ξ_i are defined by

$$\zeta_i = \frac{1}{\beta} \int_0^{\beta} \sum_{\nu=1}^{D} \zeta_{i\nu}(\tau)\, \mathrm{d}\tau \tag{17}$$

$$\xi_i = \frac{1}{\beta} \int_0^{\beta} \sum_{\nu=1}^{D} \xi_{i\nu z}(\tau)\, \mathrm{d}\tau \tag{18}$$

and the effective Coulomb and exchange energy parameters are defined as

$$\tilde{U}_i = \left[1 - \frac{1}{2D} \right] U_i + \frac{3}{2D} J_i \tag{19}$$

$$\tilde{J}_i = \frac{1}{2D} U_i + \left[1 + \frac{1}{2D} \right] J_i. \tag{20}$$

The unit vector $\boldsymbol{e}_i$ in equation (16) denotes the direction of the rotated z-axis at site i.

The partition function does not satisfy rotational invariance since we neglected the transverse spin fluctuations in the rotated coordinates. Therefore we average $Z(\{\boldsymbol{e}_i\})$ over all of the directions $\{\boldsymbol{e}_i\}$, and obtain the free energy as follows:

$$F_{\mathrm{st}} = -\beta^{-1} \int \left[\prod_i^{N} \left(\frac{\beta \tilde{J}_i}{4\pi} \right)^{1/2} \mathrm{d}\xi_i\, \mathrm{d}\boldsymbol{e}_i \right] \mathrm{e}^{-\beta E(\boldsymbol{\xi})} \tag{21}$$

$$E(\boldsymbol{\xi}) = -\beta^{-1} \ln \mathrm{Tr}(\mathrm{e}^{-\beta H_{\mathrm{st}}(\boldsymbol{\xi}, \zeta)}) - \frac{1}{4} \sum_i (\tilde{U}_i \zeta_i^2 - \tilde{J}_i \xi_i^2). \tag{22}$$

Here $\mathrm{d}\boldsymbol{e}_i = (4\pi)^{-1} \sin\theta_i\, \mathrm{d}\theta_i\, \mathrm{d}\phi_i$ and $\boldsymbol{\xi}_i = \xi_i \boldsymbol{e}_i$. We adopted the saddle-point approximation for the charge fields in H_{st}, so $\zeta_i(\boldsymbol{\xi})$ satisfies the condition $\partial E / \partial \zeta_i = 0$:

$$\zeta_i(\boldsymbol{\xi}) = \langle n_i \rangle_0 = \frac{\mathrm{Tr}(n_i \mathrm{e}^{-\beta H_{\mathrm{st}}(\boldsymbol{\xi}, \zeta)})}{\mathrm{Tr}(\mathrm{e}^{-\beta H_{\mathrm{st}}(\boldsymbol{\xi}, \zeta)})} \tag{23}$$

where $\langle n_i \rangle_0$ denotes the thermal average with respect to H_{st}. It should be noted that the free energy (21) reduces to that of the generalized Hartree–Fock approximation at the ground state.

We introduce here, according to Hubbard [4], the charge potential $w_i(\boldsymbol{\xi})$ defined as

$$w_i(\boldsymbol{\xi}) = \frac{1}{2} \tilde{U} (\zeta_i(\boldsymbol{\xi}) - \zeta_i^0). \tag{24}$$

Here ζ_i^0 is a constant. The saddle-point condition $\partial E/\partial \zeta_i = 0$ reduces to $\partial E/\partial w_i = 0$, which leads to the condition

$$\zeta_i^0 = \langle n_i \rangle_0 \big(\{ \epsilon_j^0 - \mu - w_j(\boldsymbol{\xi}) \} \big) - \frac{2}{\tilde{U}} w_i(\boldsymbol{\xi}). \tag{25}$$

We choose ζ_i^0 such that $\{w_i(\boldsymbol{\xi})\}$ vanish at $T = 0$: $\zeta_i^0 = \langle n_i \rangle_0 (\{\epsilon_j^0 - \mu\})$.

In the strong-$\tilde{U}$ limit, the charge-neutrality condition $\zeta_i^0 = n_i$ can be satisfied at each site, where n_i on the right-hand side denotes the average electron number of the pure metal for the atom at site i. Therefore equation (25) for determining the charge potential reduces to the following equation in the strong-$\tilde{U}$ limit:

$$n_i = \langle n_i \rangle_0 \big(\{ \epsilon_j^0 - \mu - w_j(\boldsymbol{\xi}) \} \big). \tag{26}$$

The energy $E(\boldsymbol{\xi})$ in equation (22) then reduces to

$$E(\boldsymbol{\xi}) = \int \mathrm{d}\omega \, f(\omega) \frac{1}{\pi} \operatorname{Im} \operatorname{Tr} \ln(L^{-1} - t) - \sum_i n_i w_i(\boldsymbol{\xi}) + \sum_i \frac{1}{4} \tilde{J}_i \xi_i^2 \tag{27}$$

$$(L^{-1})_{i\nu\sigma j\nu'\sigma'} = (\omega + \mathrm{i}\delta - \epsilon_i^0 + \mu - w_i(\boldsymbol{\xi}))\delta_{ij}\delta_{\nu\nu'}\delta_{\sigma\sigma'} + \frac{1}{2}\tilde{J}_i \boldsymbol{\xi}_i \cdot (\boldsymbol{\sigma})_{\sigma\sigma'}\delta_{ij}\delta_{\nu\nu'} \tag{28}$$

where $f(\omega)$ is the Fermi distribution function and the constant term has been dropped.

Using the expression for the free energy given as equation (21), various thermodynamic quantities can be calculated. The local magnetic moment (LM) is expressed in a semi-classical form as

$$\langle \boldsymbol{m}_i \rangle = \left\langle \left(1 + \frac{4}{\beta \tilde{J}_i \xi_i^2} \right) \boldsymbol{\xi}_i \right\rangle. \tag{29}$$

The local charge fluctuations $\langle n_i^2 \rangle$ and the amplitude of the LMs at site i are given by

$$\langle n_i^2 \rangle = n_i + \left(1 - \frac{1}{2D} \right) n_i^2 - \frac{1}{2D} \left(\langle \xi_i^2 \rangle - \frac{2}{\beta \tilde{J}_i} \right) \tag{30}$$

$$\langle \boldsymbol{m}_i^2 \rangle = 3n_i - \frac{3}{2D} n_i^2 + \left(1 + \frac{1}{2D} \right) \left(\langle \xi_i^2 \rangle - \frac{2}{\beta \tilde{J}_i} \right). \tag{31}$$

The average $\langle \sim \rangle$ on the right-hand side of the above equations is defined by

$$\langle \sim \rangle = \left(\int \left[\prod_i \mathrm{d}\boldsymbol{\xi}_i \right] (\sim) \mathrm{e}^{-\beta \Psi(\boldsymbol{\xi})} \right) \Big/ \left(\int \left[\prod_i \mathrm{d}\boldsymbol{\xi}_i \right] \mathrm{e}^{-\beta \Psi(\boldsymbol{\xi})} \right) \tag{32}$$

$$\Psi(\boldsymbol{\xi}) = E(\boldsymbol{\xi}) + 2T \sum_i \ln \xi_i. \tag{33}$$

Note that we adopted spherical coordinates in the above average, $\langle \sim \rangle$.

It is noted that the disorder of the LMs originates from the spatial fluctuations of the atomic level $\{\epsilon_i^0\}$ and the transfer integrals $\{t_{i\nu j\nu'}\}$ in the substitutional binary alloys. The off-diagonal disorder associated with the transfer integral is important when the relative bandwidths of the constituent atoms A and B are considerably different. We consider in the following a geometrical-mean model for the transfer integrals.

If the constituent metals A and B have similar energy bands, one can write the transfer integral $t_{i\nu j\nu'}$ as

$$t_{i\nu j\nu'} = r_\lambda^* t_{i\nu j\nu'}^0 r_{\lambda'} \tag{34}$$

where $t^0_{i\nu j\nu'}$ represents the transfer integral of pure metal B, which is expressed as a linear combination of the Slater–Koster parameters for the B atom, $\mathrm{dd}\sigma^{\mathrm{BB}}$, $\mathrm{dd}\pi^{\mathrm{BB}}$ and $\mathrm{dd}\delta^{\mathrm{BB}}$. The parameter $|r_\lambda|$ is defined as

$$|r_\lambda| = \sqrt{\frac{(\mathrm{dd}m)^{\lambda\lambda}}{(\mathrm{dd}m)^{\mathrm{BB}}}} \tag{35}$$

which depends on the type λ of the atom at site i. If site i is occupied by an A atom, $|r_\lambda|^2$ is the ratio of the bandwidth of pure metal A to that of metal B; otherwise, it is 1.

The single-site approximation (SSA) [4–8] provides us with the simplest scheme for evaluating the thermal average of LM (29) at finite temperatures. The LM at site i is regarded as an impurity in an effective medium $\mathcal{L}_\sigma^{-1}$, so the average LM and its amplitude for atom λ are expressed as

$$[\langle \boldsymbol{m}_\lambda \rangle]_{\mathrm{c}} = \left(\int \left(\frac{\beta \tilde{J}_\lambda}{4\pi} \right)^{1/2} \mathrm{d}\boldsymbol{\xi}\ \xi^{-2} \left(1 + \frac{4}{\beta \tilde{J}_\lambda \xi^2} \right) \boldsymbol{\xi} \mathrm{e}^{-\beta E_\lambda(\boldsymbol{\xi})} \right) \times \left(\int \left(\frac{\beta \tilde{J}_\lambda}{4\pi} \right)^{1/2} \mathrm{d}\boldsymbol{\xi}\ \xi^{-2} \mathrm{e}^{-\beta E_\lambda(\boldsymbol{\xi})} \right)^{-1} \tag{36}$$

$$\left[\langle \boldsymbol{m}_\lambda^2 \rangle \right]_{\mathrm{c}} = 3n_\lambda - \frac{3}{2D} n_\lambda^2 + \left(1 + \frac{1}{2D} \right) \left([\langle \xi_\lambda^2 \rangle]_{\mathrm{c}} - \frac{2}{\beta \tilde{J}_\lambda} \right) \tag{37}$$

where $[\ ]_{\mathrm{c}}$ represents the configurational average over sites.

$$E_\lambda(\boldsymbol{\xi}) = \int \mathrm{d}\omega\ f(\omega) \frac{1}{\pi} \operatorname{Im} \sum_\Gamma d_\Gamma \ln \det{}_{\lambda\Gamma}(\omega + \mathrm{i}\delta, \xi_z, \xi_\perp^2) - n_\lambda w_\lambda(\boldsymbol{\xi}) + \frac{1}{4} \tilde{J}_\lambda \xi^2 \tag{38}$$

$$\det{}_{\lambda\Gamma}(\omega + \mathrm{i}\delta, \xi_z, \xi_\perp^2) = (\hat{L}_{\lambda\uparrow}^{-1} - \mathcal{L}_\uparrow^{-1} + F_{\Gamma\uparrow}^{-1})(\hat{L}_{\lambda\downarrow}^{-1} - \mathcal{L}_\downarrow^{-1} + F_{\Gamma\downarrow}^{-1}) - |r_\lambda|^{-4} \frac{1}{4} \tilde{J}_\lambda^2 \xi_\perp^2 \tag{39}$$

$$\hat{L}_{\lambda\sigma}^{-1} = |r_\lambda|^{-2} \left(\omega + \mathrm{i}\delta - \epsilon_0 + \mu - w_\lambda(\boldsymbol{\xi}) + \frac{1}{2} \tilde{J}_\lambda \xi_z \sigma \right). \tag{40}$$

Here we have adopted a site-independent effective medium. The quantities δ and $\xi_\perp$ represent an infinitesimal positive number and the transverse component of the field variable respectively. d_Γ is the number of orbitals ν belonging to the same irreducible representation Γ of the point symmetry in the crystal.

The diagonal coherent Green function $F_{\Gamma\sigma}$ in equation (39) is given by

$$F_{\Gamma\sigma} = \left[(\mathcal{L}^{-1} - t^0)^{-1} \right]_{i\Gamma\nu\sigma, i\Gamma\nu\sigma} = \int \frac{\hat{\rho}_\Gamma(\epsilon)\ \mathrm{d}\epsilon}{\mathcal{L}_\sigma^{-1} - \epsilon}. \tag{41}$$

Here we assumed that all of the sites on the Bravais lattice are equivalent to each other. $\hat{\rho}_\Gamma(\epsilon)$ is the noninteracting DOS for an orbital belonging to the irreducible representation Γ for the pure metal B.

The magnetization and the average amplitude of LM at the concentration $\{c_\lambda\}$ are given by

$$[\langle \boldsymbol{m} \rangle]_{\mathrm{c}} = \sum_\lambda c_\lambda [\langle \boldsymbol{m}_\lambda \rangle]_{\mathrm{c}} \tag{42}$$

$$[\langle \boldsymbol{m}^2 \rangle]_{\mathrm{c}} = \sum_\lambda c_\lambda [\langle \boldsymbol{m}_\lambda^2 \rangle]_{\mathrm{c}}. \tag{43}$$

The charge potentials $w_\lambda(\boldsymbol{\xi})$ are calculated from the charge-neutrality condition (26):

$$n_\lambda = \int \mathrm{d}\omega\ f(\omega) \frac{(-1)}{\pi} \operatorname{Im} \sum_{\Gamma\sigma} d_\Gamma G_{\lambda\Gamma\sigma}(\omega + \mathrm{i}\delta, \xi_z, \xi_\perp^2, \mathcal{L}^{-1}). \tag{44}$$

Here $G_{\lambda\Gamma\sigma}(\omega+\mathrm{i}\delta,\xi_z,\xi_\perp^2,\mathcal{L}^{-1})$ is the impurity Green function defined as

$$G_{\lambda\Gamma\sigma}(\omega+\mathrm{i}\delta,\xi_z,\xi_\perp^2,\mathcal{L}^{-1})=|r_\lambda|^{-2}\left(\hat{L}_{\lambda\sigma}^{-1}-\mathcal{L}_{\lambda\sigma}^{-1}+F_{\Gamma\sigma}^{-1}-\frac{[1/(4|r_\lambda|^4)]\tilde{J}_\lambda^2\xi_\perp^2}{(\hat{L}_{\lambda-\sigma}^{-1}-\mathcal{L}_{-\sigma}^{-1}+F_{\Gamma-\sigma}^{-1})}\right)^{-1}. \tag{45}$$

The effective medium $\mathcal{L}_\sigma^{-1}(z)$ is determined self-consistently [2] via the following CPA equation:

$$\sum_{\lambda\Gamma}c_\lambda\frac{d_\Gamma}{D}\sum_{q=\pm1}\frac{1}{2}\left(1+q\frac{[\langle\xi_{\lambda z}\rangle]_\mathrm{c}}{[\langle\xi_{\lambda z}^2\rangle]_\mathrm{c}^{1/2}}\right)|r_\lambda|^2G_{\Gamma\lambda\sigma}(\omega+\mathrm{i}\delta,q[\langle\xi_{\lambda z}^2\rangle]_\mathrm{c}^{1/2},[\langle\xi_{\lambda\perp}^2\rangle]_\mathrm{c},\mathcal{L}^{-1})$$
$$=\sum_\Gamma\frac{d_\Gamma}{D}F_{\Gamma\sigma}. \tag{46}$$

Here the quantities $[\langle\xi_{\lambda z}\rangle]_\mathrm{c}$, $[\langle\xi_{\lambda z}^2\rangle]_\mathrm{c}$, and $\langle\xi_{\lambda\perp}^2\rangle]_\mathrm{c}$ are determined self-consistently.

The single-site theory at finite temperatures is useful for the description of systems with simple magnetic structures. For complex magnetic structure one has to introduce a site-dependent effective medium in the theory. The determination of the effective medium, however, would be difficult due to the lack of information about the direction of the polarization at each site. To avoid this difficulty and to treat the problem more exactly, we apply the molecular dynamics (MD) method to substitutional magnetic alloys with complex magnetic structures in the following section.

2.2. Applying the molecular dynamics method to substitutional magnetic alloys

The thermal average of the LM in equation (29) has a semi-classical form described by a potential energy $\Psi(\boldsymbol{\xi})$. In order to determine the magnetic structures of the alloys, we adopt the temperature control MD method with an extended system [11, 12], assuming ergodicity of the system, and calculate the thermal averages of LM (29) by means of time averaging of the fictitious LM $\boldsymbol{\xi}_i(t)$:

$$\langle\boldsymbol{m}_i\rangle=\lim_{t_0\to\infty}\frac{1}{t_0}\int_0^{t_0}\left(1+\frac{4}{\beta\tilde{J}_i\xi_i^2(t)}\right)\boldsymbol{\xi}_i(t)\ \mathrm{d}t. \tag{47}$$

The equations of motion leading to the classical ensemble described by $\Psi(\boldsymbol{\xi})$ are given by

$$\dot{\xi}_{i\alpha}=\frac{p_{i\alpha}}{\mu_\mathrm{LM}} \tag{48}$$

$$\dot{p}_{i\alpha}=-\frac{\partial\Psi(\boldsymbol{\xi})}{\partial\xi_{i\alpha}}-\eta_\alpha p_{i\alpha} \tag{49}$$

$$\dot{\eta}_\alpha=\frac{1}{Q}\left(\sum_i\frac{p_{i\alpha}^2}{\mu_\mathrm{LM}}-NT\right). \tag{50}$$

Here $p_{i\alpha}$ is the momentum conjugate to the fictitious LM $\xi_{i\alpha}$ at site i, and η_α is a thermodynamic friction coefficient. μ_LM and Q are the effective-mass parameters for the LM at site i and the thermal variable η_α respectively. N in equation (50) is the number of LMs in the system.

We introduced three independent variables η_α instead of a uniform friction coefficient η in the above equations, so that the ergodic assumption is not violated even when the MD method is applied to the impurity problem.

The first term of equation (49) represents the magnetic force given by

$$-\frac{\partial\Psi(\boldsymbol{\xi})}{\partial\xi_{i\alpha}} = \frac{1}{2}\tilde{J}_i(\langle m_{i\alpha}\rangle_0 - \xi_{i\alpha}) - \frac{2T\xi_{i\alpha}}{\xi_i^2}. \tag{51}$$

Here $\langle m_{i\alpha}\rangle_0$ is the average magnetic moment at site i with respect to the one-electron Hamiltonian in random exchange fields. Note that equation (51) yields the generalized Hartree–Fock equation $\partial\Psi(\boldsymbol{\xi})/\partial\xi_{i\alpha} = 0$ at $T = 0$. The second term in equation (49) describes the effect of the heat bath used to keep the temperature constant by changing the coefficient η_α according to equation (50).

The average magnetic moment $\langle m_{i\alpha}\rangle_0$ in equation (51) is written as the imaginary part of the Green function:

$$\langle m_{i\alpha}\rangle_0 = \int \mathrm{d}\omega\ f(\omega)\frac{(-1)}{\pi}\mathrm{Im}\sum_{\nu\sigma}(\sigma_\alpha G)_{i\nu\sigma i\nu\sigma} \tag{52}$$

where

$$G = (L^{-1} - t)^{-1}. \tag{53}$$

The products $(\sigma_\alpha G)_{i\nu\sigma i\nu\sigma}$ in equation (52) are expressed by means of the diagonal Green functions in the representation which diagonalizes the Pauli spin matrix σ_α ($\alpha = x, y, z$):

$$\sum_\sigma(\sigma_x G)_{i\nu\sigma i\nu\sigma} = G_{i\nu 1 i\nu 1} - G_{i\nu 2 i\nu 2} \tag{54}$$

$$\sum_\sigma(\sigma_y G)_{i\nu\sigma i\nu\sigma} = G_{i\nu 3 i\nu 3} - G_{i\nu 4 i\nu 4} \tag{55}$$

$$\sum_\sigma(\sigma_z G)_{i\nu\sigma i\nu\sigma} = G_{i\nu\uparrow i\nu\uparrow} - G_{i\nu\downarrow i\nu\downarrow}. \tag{56}$$

Here

$$|i\nu 1\rangle = \frac{1}{\sqrt{2}}(|i\nu\uparrow\rangle + |i\nu\downarrow\rangle) \tag{57}$$

$$|i\nu 2\rangle = \frac{1}{\sqrt{2}}(|i\nu\uparrow\rangle - |i\nu\downarrow\rangle) \tag{58}$$

$$|i\nu 3\rangle = \frac{1}{\sqrt{2}}(|i\nu\uparrow\rangle + \mathrm{i}|i\nu\downarrow\rangle) \tag{59}$$

$$|i\nu 4\rangle = \frac{1}{\sqrt{2}}(|i\nu\uparrow\rangle - \mathrm{i}|i\nu\downarrow\rangle). \tag{60}$$

The diagonal Green function $G_{i\nu\alpha i\nu\alpha}$ ($\alpha = 1$–$4, \uparrow, \downarrow$) can be calculated using the recursion method [24, 25], and is expressed as a continued fraction as follows:

$$G_{i\nu\alpha i\nu\alpha} = \cfrac{1}{\omega + \mathrm{i}\delta - a_{1i\nu\alpha}(\boldsymbol{\xi}) - \cfrac{|b_{1i\nu\alpha}(\boldsymbol{\xi})|^2}{\omega + \mathrm{i}\delta - a_{2i\nu\alpha}(\boldsymbol{\xi}) - \cfrac{|b_{2i\nu\alpha}(\boldsymbol{\xi})|^2}{\cdots \cfrac{\cdots}{\cdots - \cfrac{|b_{l-1i\nu\alpha}(\boldsymbol{\xi})|^2}{\omega + \mathrm{i}\delta - a_{li\nu\alpha}(\boldsymbol{\xi}) - T_{li\nu\alpha}}}}}}. \tag{61}$$

Here $a_{li\nu\alpha}(\boldsymbol{\xi})$ and $b_{li\nu\alpha}(\boldsymbol{\xi})$ are the recursion coefficients of the lth order. $T_{li\nu\alpha}$ is the terminator at the lth level.

At the present stage, we can treat a few hundred atoms at maximum in our MD method due to the limited memory and computing time of our computer. We therefore extend the system by adopting periodic boundary conditions and perform the MD simulation for N atoms in a cubic unit cell. For random alloys, we determine the random atomic configuration in the unit cell as follows to realize an alloy with a given concentration c_λ and a given atomic short-range-order parameter τ_{SRO}, which is defined by

$$p^{\mathrm{AA}} = c_{\mathrm{A}} + c_{\mathrm{B}}\tau_{\mathrm{SRO}}. \tag{62}$$

Here p^{AA} denotes the probability of finding an A atom as the nearest neighbour of another A atom.

We first create an A or B atom at each site with the probability c_{A} or c_{B} using random numbers. Next, we replace an A atom with a B atom (or a B atom with an A atom) at randomly chosen sites until the given concentration c_{A} is realized. Third, we calculate the probability $\tilde{p}^{\mathrm{AA}} = \sum_{i\in\mathrm{A}} N_{\mathrm{AA}}(i)/N_{\mathrm{A}}z$, i.e. the probability of finding an A atom at the neighbouring site of another A atom for the atomic configuration produced above. Here $N_{\mathrm{AA}}(i)$ denotes the number of A atoms at the nearest-neighbour sites of the A atom at site i, z is the number of nearest-neighbour sites, and N_{A} is the total number of A atoms among N atoms in the unit cell. If the probability $\tilde{p}^{\mathrm{AA}}$ is smaller (larger) than p^{AA}, we exchange the A atom with the B atom in a randomly chosen A–B pair, and accept the exchange if the new $\tilde{p}^{\mathrm{AA}}$ is larger (smaller) than the old one. We obtain the alloy by repeating the procedure until $|\tilde{p}^{\mathrm{AA}} - p^{\mathrm{AA}}| \leqslant \varepsilon$ $(=2/Nz)$ is satisfied.

We can allocate the atomic and exchange potentials $\epsilon_i^0 + \mu - w_i(\boldsymbol{\xi})$ and $-\tilde{J}_i\boldsymbol{\xi}_i \cdot \boldsymbol{\sigma}/2$ as well as the transfer integrals given by (34) on the Bravais lattice according to the atomic configuration determined above. Therefore we can calculate the Green function (61) by using the recursion method at each MD step.

The periodicity of the LMs in the MD approach causes artificial magnetic forces due to self-interactions and double-counting interactions via the recursion coefficients in equation (61) due to the existence of equivalent LMs in different unit cells. This difficulty may be removed by replacing the terminator with an effective one at the lowest lth recursion level, where the artificial interactions appear first due to the periodic boundary conditions; we replace there the terminator $T_{liv\alpha}$ with the terminator of the coherent Green function $[(\mathcal{L}^{-1} - t^0)^{-1}]_{iv\alpha iv\alpha}/|r_i|^2$ by making the following approximation:

$$T_{liv\alpha} \approx |r_\lambda|^2 \mathcal{T}_{lv\alpha}. \tag{63}$$

Here $\mathcal{T}_{lv\alpha}$ is the terminator of the lth level obtained from the coherent Green function (41).

The actual calculations of $\mathcal{T}_{lv\alpha}$ for $\alpha = 1$–4 are time consuming because the recursion coefficients depend on the energy due to the off-diagonal elements in spin space. We therefore adopt the following simpler expression for $\alpha = 1$–4:

$$\mathcal{T}_{lv\alpha} = \mathcal{T}_{lv} + \frac{(\hat{h} - \Delta_{lv})^2}{\hat{\mathcal{L}}^{-1} - \mathcal{T}_{lv}}. \tag{64}$$

Here

$$\mathcal{T}_{lv} = \frac{1}{2}(\mathcal{T}_{lv\uparrow} + \mathcal{T}_{lv\downarrow}) \tag{65}$$

$$\Delta_{lv} = \frac{1}{2}(\mathcal{T}_{lv\uparrow} - \mathcal{T}_{lv\downarrow}) \tag{66}$$

$$\hat{\mathcal{L}}^{-1} = \frac{1}{2}(\mathcal{L}_\uparrow^{-1} + \mathcal{L}_\downarrow^{-1}) \tag{67}$$

$$\hat{h} = \frac{1}{2}(\mathcal{L}_\uparrow^{-1} - \mathcal{L}_\downarrow^{-1}). \tag{68}$$

The above relation for $\mathcal{T}_{lv\alpha}$ is reasonable for $l = 1$ in the polarized medium and for all l in the nonpolarized medium. The effective medium $\mathcal{L}_\sigma^{-1}$ is determined by solving the CPA equation.

We approximate the charge potential by the single-site one for brevity, and transform equation (44) into the equation of motion for the charge potential $w_i(\boldsymbol{\xi})$ as follows:

$$\dot{w}_{\rm i} = \sum_\alpha \frac{C_{\lambda\alpha}(\boldsymbol{\xi}_i)p_{i\alpha}}{\mu_{\rm LM}} \tag{69}$$

where

$$C_{\lambda\alpha}(\boldsymbol{\xi}) = \frac{\tilde{J}_\lambda}{2B_\lambda(\boldsymbol{\xi})}\int {\rm d}\omega\ f(\omega)\frac{(-1)}{\pi}\,{\rm Im}\sum_\Gamma d_\Gamma G_{\lambda\Gamma\alpha}(G_{\lambda\Gamma\uparrow}+G_{\lambda\Gamma\downarrow}) \tag{70}$$

$$B_\lambda(\boldsymbol{\xi}) = \int {\rm d}\omega\ f(\omega)\frac{(-1)}{\pi}\,{\rm Im}\sum_{\Gamma\sigma} d_\Gamma\left[{G_{\lambda\Gamma\sigma}}^2 + \left(\frac{\tilde{J}_\lambda\xi_\perp}{2|r_\lambda|^4\ {\rm det}_{\lambda\Gamma}}\right)^2\right]. \tag{71}$$

Note that the initial values $\{w_i(\boldsymbol{\xi}_i(0))\}$ should satisfy equation (44).

In summary, the self-consistent MD method for substitutional magnetic alloys is realized by taking the following steps. First, we determine the random atomic configuration for the alloys and adopt the bandwidths of the pure metals to calculate the off-diagonal factors $|r_\lambda|^2$ using equation (35). Second, we take $[\langle\xi_{\lambda z}\rangle]_{\rm c}$, $[\langle\xi_{\lambda z}^2\rangle]_{\rm c}$, $[\langle\xi_{\lambda\perp}^2\rangle]_{\rm c}$, and the charge potentials $w_\lambda(\boldsymbol{\xi})$ for $\xi_z = \pm[\langle\xi_{\lambda z}^2\rangle]_{\rm c}^{1/2}$, $\xi_\perp^2 = [\langle\xi_{\lambda\perp}^2\rangle]_{\rm c}$, within the single-site approximation, and solve the CPA equation (46) for the effective medium $\mathcal{L}_\sigma^{-1}$. Then we calculate the coherent Green function $F_{\Gamma\sigma}$ and the effective terminators $\mathcal{T}_{lv\alpha}$ from the effective medium. Next, we solve the equations of motion of LMs (48)–(50) in the course of which we calculate the magnetic force (51) using the recursion method at each time step. After obtaining the stationary MD data we again calculate $[\langle\xi_{\lambda z}\rangle]_{\rm c}$, $[\langle\xi_{\lambda z}^2\rangle]_{\rm c}$, $[\langle\xi_{\lambda\perp}^2\rangle]_{\rm c}$, and $w_\lambda(\boldsymbol{\xi})$ for $\xi_z = \pm[\langle\xi_{\lambda z}^2\rangle]_c^{1/2}$, and $\xi_\perp^2 = [\langle\xi_{\lambda\perp}^2\rangle]_c^{1/2}$. If the new output values are consistent with the input, we calculate the magnetic moments of the alloys at finite temperatures using equation (47).

3. Numerical results

We have calculated the magnetic structures and the magnetic moments of disordered γ-FeMn alloys over all concentrations at low temperatures applying the MD approach described in the last section. We adopted the Slater–Koster parameters used by Pettifor [26] with the bandwidths 0.390 Ryd for γ-Fe and 0.443 Ryd for γ-Mn [1]. The exchange energy parameters are chosen to be 0.065 Ryd [27] and 0.060 Ryd [28], and the d-electron numbers are 7.0 and 6.25 for γ-Fe and γ-Mn, respectively. The effective medium was not determined self-consistently in the present calculations; we adopted the medium obtained by using the single-site approximation over all concentrations for brevity. Moreover, we adopted $N = 108$ atoms per MD unit cell (a $3 \times 3 \times 3$ fcc lattice).

In the numerical integrations for equations (48)–(50) and (69) we used the Runge–Kutta method to the fourth order. The size of the time step was chosen as $\Delta t \approx 0.01 T_{\rm LM}$. Here $T_{\rm LM}$ represents a characteristic time of fluctuations for LMs defined by

$$T_{\rm LM} = 2\pi\left(\frac{2\mu_{\rm LM}}{c_{\rm A}\tilde{J}_{\rm A} + c_{\rm B}\tilde{J}_{\rm B}}\right)^{1/2}. \tag{72}$$

We adopted the parameter $\mu_{\rm LM} = 1$ and the parameter Q obtained from the condition that

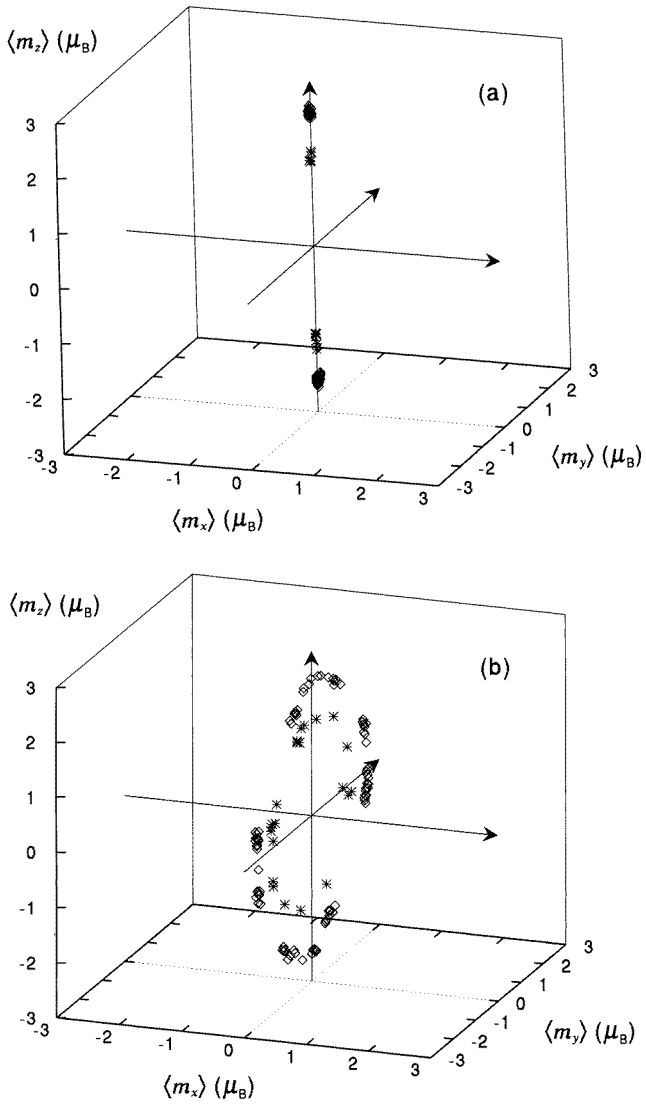

Figure 1. The distribution of local magnetic moments (LMs) for γ-FeMn alloys at various concentrations obtained by the MD approach at 25 K: (a) 10 at.% Fe; (b) 20 at.% Fe; (c) 30 at.% Fe; (d) 50 at.% Fe; (e) 65 at.% Fe; (f) 80 at.% Fe; and (g) 90 at.% Fe. The symbols $\diamond$ and $*$ represent the Fe LMs and Mn LMs respectively.

the characteristic time of the LM agrees with that of the friction coefficient expressed by

$$T_\eta = 2\pi \left(\frac{Q}{2NT} \right)^{1/2}. \tag{73}$$

It is noted that the initial configuration of $\{\xi_{i\alpha}, p_{i\alpha}, \eta_\alpha\}$ should have no influence whatever on the result of the simulation in principle. The following choice of the initial values, however, may lead to a quick approach to the stationary state, since these values

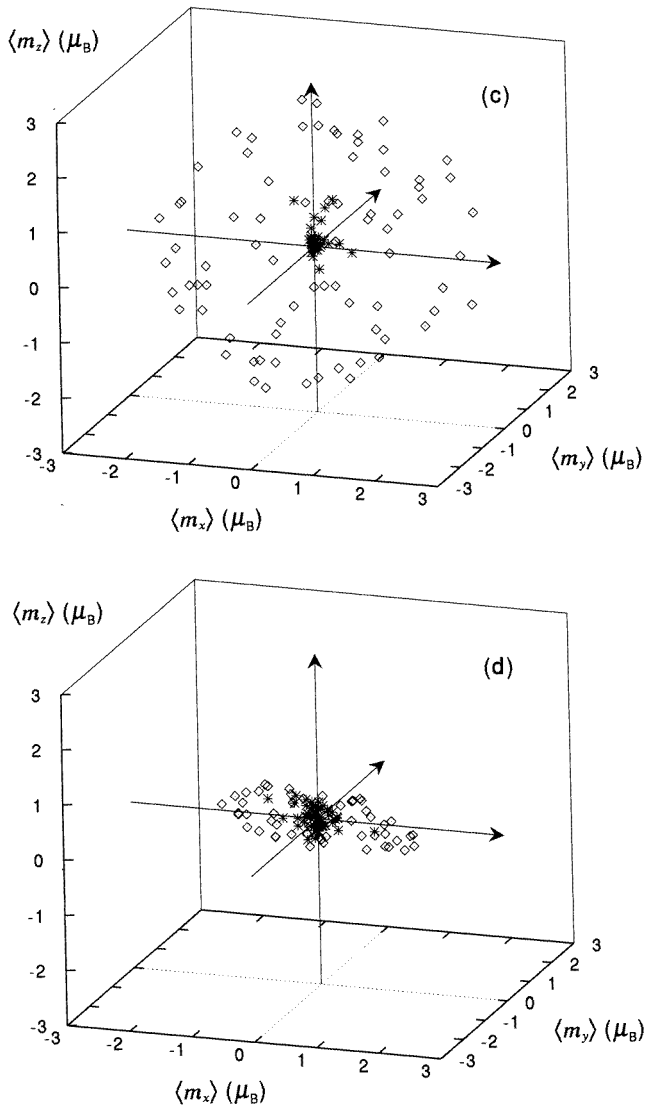

Figure 1. (Continued)

are expected to be close to the average value in the stationary state:

$$\xi_{i\alpha}(0) = \pm\left(\frac{\langle \xi_{\lambda\perp}{}^2\rangle_{\rm in}}{2}\right)^{1/2} \qquad (\alpha = x, y) \tag{74}$$

$$\xi_{iz}(0) = \langle \xi_{\lambda z}\rangle_{\rm in} \pm (\langle \xi_{\lambda z}^2\rangle_{\rm in} - \langle \xi_{\lambda z}\rangle_{\rm in}^2)^{1/2} \tag{75}$$

$$p_{i\alpha}(0) = \pm(\mu_{\rm LM} T)^{1/2} \tag{76}$$

$$\eta_\alpha(0) = \pm\left(\frac{T}{Q}\right)^{1/2}. \tag{77}$$

Here $\langle \xi_{\lambda z}\rangle_{\rm in}$, $\langle \xi_{\lambda z}^2\rangle_{\rm in}$, and $\langle \xi_{\lambda\perp}{}^2\rangle_{\rm in}$ are the input values for the CPA calculations, and the

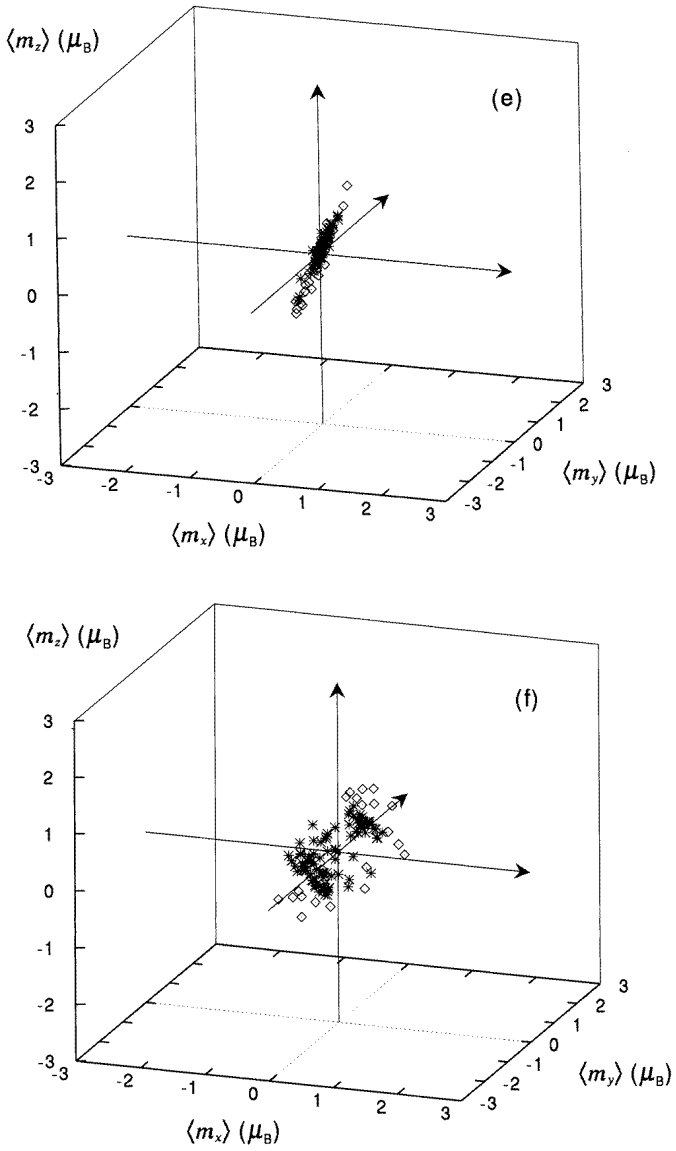

Figure 1. (Continued)

sign $\pm$ is determined randomly using random numbers. Starting from the random atomic configuration of LMs mentioned above, we solved the equations of motion (48)–(50) and (69) typically up to 6000 steps at 25 K for each concentration. The stationary states are realized after a thousand MD steps in most cases.

3.1. Magnetic structure

Figures 1(a)–1(f) and 2(a)–2(h) show the distributions of magnetic moments and the magnetic structures calculated at 25 K for various concentrations, respectively. γ-Mn shows

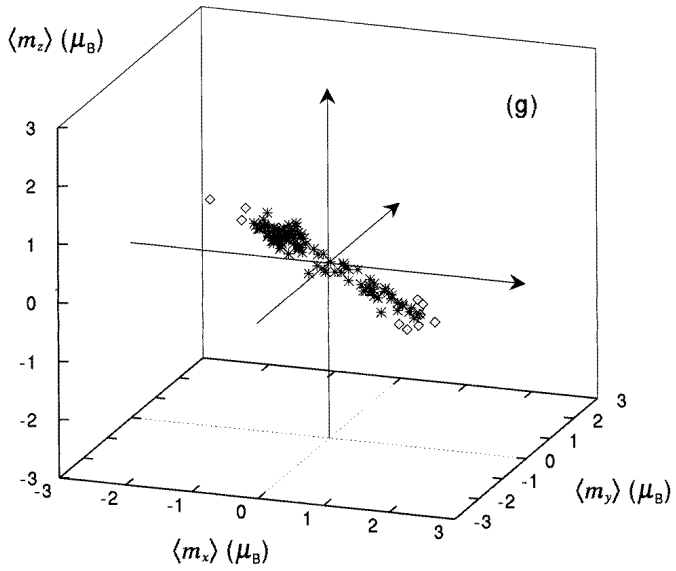

Figure 1. (Continued)

the first-kind antiferromagnetic structure in agreement with experiments [14, 29]. When Fe atoms are added to γ-Mn, the Fe magnetic moments are arranged without violation of the AFI structure. The magnitude of the Fe LM is calculated as $1.65\mu_B$ in the impurity limit, which is smaller than the calculated Mn LM: $2.4\mu_B$. This feature does not change up to 10 at.% Fe as shown in figures 1(a) and 2(a).

The collinear AF structure starts to collapse beyond 10 at.% Fe and changes to a helix-like structure as shown in figures 1(b) and 2(b), which are obtained at 20 at.% Fe. The structure obtained at 20 at.% Fe may be regarded as a mixture of two kinds of helical structure with the wave vectors $\boldsymbol{Q} = (0, 1/3, 1)\,2\pi/a$ and $\boldsymbol{Q}' = (0, 1/2, 1)\,2\pi/a$, so the LMs on the three AF planes remain collinear and those on the other AF planes rotate on the planes. The helical structure with $\boldsymbol{Q} = (0, 1/3, 1)\,2\pi/a$ was obtained in the earlier rigid-band calculation for the d-electron number $n_d = 6.4$, which corresponds to the 20 at.% Fe alloy [9]. The alloying effect is therefore considered to be partly that of maintaining the collinear AF planes and partly that of causing the distribution of the directions of the LMs.

The AF planes are almost destroyed at around 30 at.% Fe, and a noncollinear structure which cannot be expressed in terms of simple $\boldsymbol{Q}$-vectors is obtained as shown in figures 1(c) and 2(c). Although the Mn LMs still have a large value ($2.5\mu_B$) there, the Fe LMs show a small value ($0.5\mu_B$). The structure at 40 at.% Fe is also noncollinear, but the Mn LMs rapidly decrease there and take a small value ($1.5\mu_B$). At 50 at.% Fe, the magnetic structure shows a noncollinear structure with large-amplitude fluctuations as well as directional fluctuations, as shown in figures 1(d) and 2(d). The concentration 50 at.% Fe corresponds to the average d-electron number 6.625. The magnetic structure obtained by the rigid-band calculations for d-electron number $n_d = 6.6$ was found to be the helical structure with amplitude fluctuations from $0.75\mu_B$ to $1.3\mu_B$ [9]. The effect of configurational disorder with competing interactions is therefore to remove the characteristic $\boldsymbol{Q}$-vector and to enhance the amplitude fluctuations. The magnetic structure at 60 at.% Fe is still noncollinear as shown in figure 2(e) though the magnitudes of LMs are enhanced.

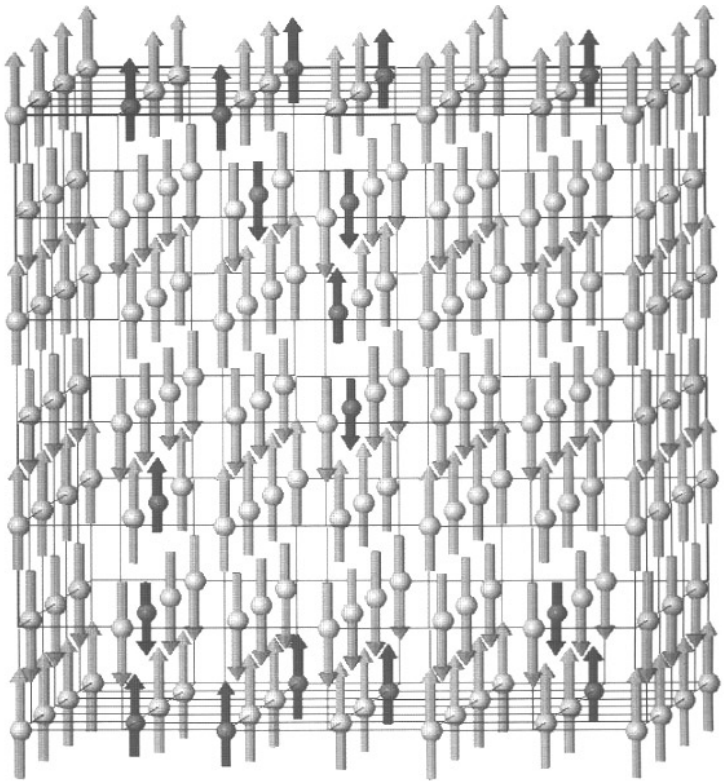

(a)

Figure 2. The magnetic structures of γ-FeMn alloys obtained by the MD method at 25 K: (a) 10 at.% Fe; (b) 20 at.% Fe; (c) 30 at.% Fe; (d) 50 at.% Fe; (e) 60 at.% Fe; (f) 70 at.% Fe; (g) 80 at.% Fe; and (h) 90 at.% Fe. The larger and white (smaller and black) spheres represent the Mn (Fe) atoms. The magnitudes of the LMs are drawn in arbitrary units.

With further increase of the Fe concentration, the magnetic structure becomes collinear-like at around 65 at.% Fe as shown in figure 1(e), and changes to the noncollinear ones shown in figure 2(f) for 70 at.% Fe and figures 1(f) and 2(g) for 80 at.% Fe. Between 85 at.% Fe and 95 at.% Fe, the collinear AF structures are stabilized as shown in figures 1(g) and 2(h) for 90 at.% Fe. The locally ferromagnetic planes are found there, while the LMs show a large distribution in magnitude (see figure 1(f)). These structures are changed to the helical structure with $\boldsymbol{Q} = (0, 1/3, 2/3)\ 2\pi/a$ beyond 95 at.% Fe [9].

The calculated magnetic structures mentioned above agree qualitatively with the experimental results. In fact, Endoh and Ishikawa [14] investigated the magnetic structures in γ-FeMn alloys using the neutron diffraction and Mössbauer techniques. They concluded that there are three different regions in the magnetic structure: the AFI collinear region between 0 and 30 at.% Fe (corresponding to our results given in figures 1(a) and 2(a)), the noncollinear region between 35 and 75 at.% Fe (corresponding to our results given in figures 1(b)–1(d) and 2(b)–2(f)), and the collinear region between 80 and 100 at.% Fe (corresponding to our results given in figures 1(g) and 2(h)). Using inelastic neutron scattering, Bisanti *et al* [16, 17] reported that fcc $Fe_{66}Mn_{34}$ alloy has a collinear magnetic structure, which may be explained by our result shown in figure 1(e). Tsunoda [13]

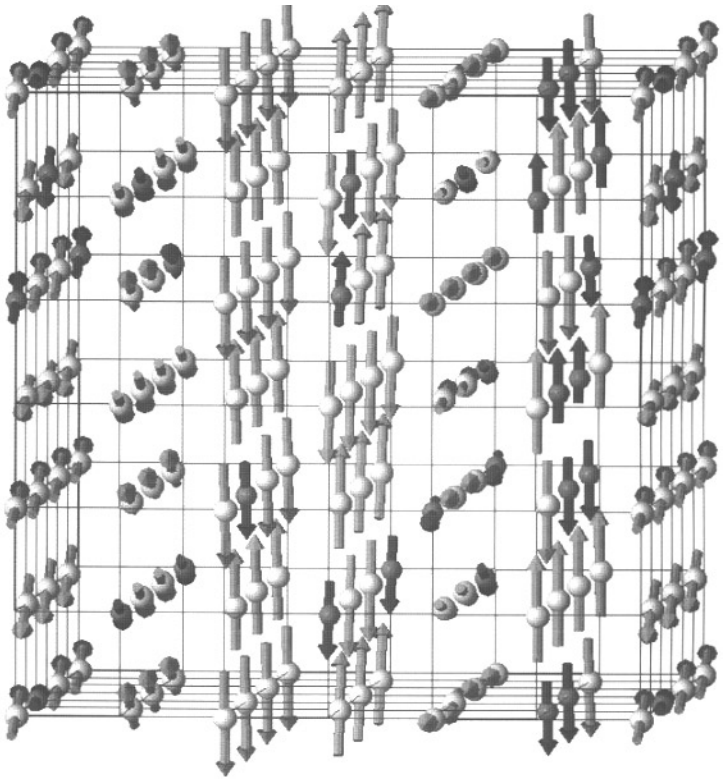

(b)

Figure 2. (Continued)

investigated the cubic γ-$Fe_{100-x}Co_x$ ($x < 4$) alloys precipitated in Cu, and suggested that γ-Fe should have the helical structure with $\boldsymbol{Q} = (0, 0.1, 1)\,2\pi/a$, which is qualitatively in agreement with our result [9].

There are some disagreements as regards the detailed magnetic structures between theory and experiment. For example, the calculated magnetic structure at 50 at.% Fe is a turbulent noncollinear magnetic structure as shown in figures 1(d) and 2(d), while a $3\boldsymbol{Q}$ spin-density wave with the wave vectors $(1, 0, 0)\,2\pi/a$, $(0, 1, 0)\,2\pi/a$, and $(0, 0, 1)\,2\pi/a$ was suggested on the basis of a neutron experiment by Endoh and Ishikawa [14]. Moreover, for the $\boldsymbol{Q}$-vector in γ-Fe there is a considerable difference between our result and experiment. The effect of considering a more detailed electronic structure, the size effect of the MD unit cell, and the effect of spin–orbit interaction need to be examined in future investigations to resolve the disagreements.

The DOS for γ-Mn with AFI structure is characterized by bonding and antibonding peaks due to the local exchange splitting, which generally stabilizes the structure in the systems with nearly half-filled bands [18]. This feature persists in the DOS at 10 and 20 at.% Fe as shown in figures 3(a) and 3(b). The small dip near the Fermi level as well as the bonding–antibonding structure seem to stabilize the magnetic structures in Mn-rich alloys. The DOS above 50 at.% Fe are characterized by the deep valley at the Fermi level in the magnetic state and a sharp peak at the Fermi level in the nonmagnetic state as shown in figures 3(c) and 3(d) for the concentrations 50 and 60 at.% Fe respectively. This feature

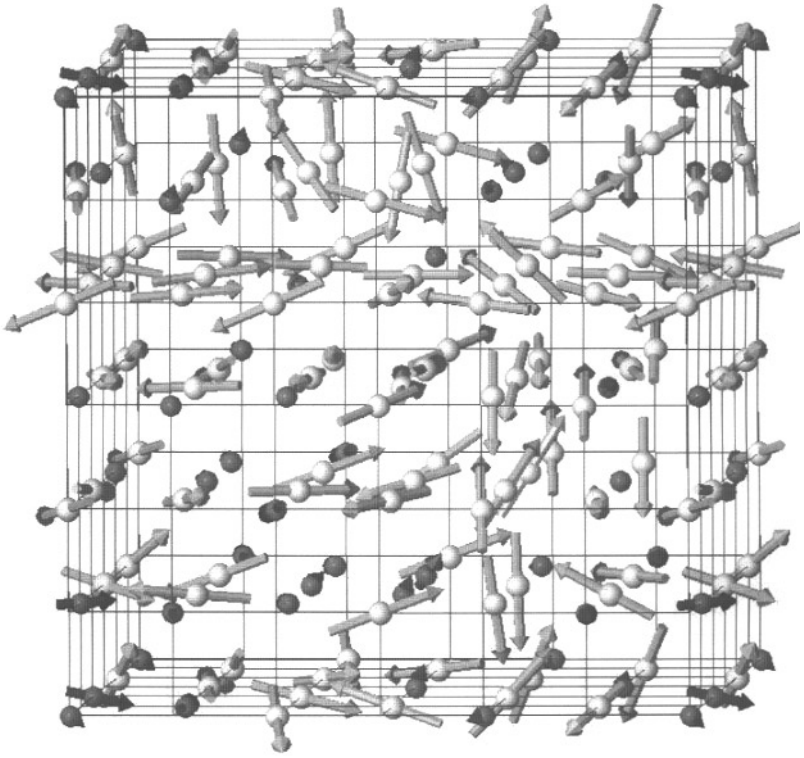

(c)

Figure 2. (Continued)

stabilizes the structures obtained in our calculations. In particular, the associated kinetic energy gain seems to become a maximum at 60 at.% Fe since the Fermi level lies just at the sharp nonmagnetic peak at this concentration and the DOS in the magnetic state creates a deeper valley. It may also explain the enhancement of the average magnetic moments at 60 at.% Fe.

3.2. Magnetic moments

Various calculated magnetic moments are presented in figure 4 together with the experimental data [14]. When Fe atoms are added to γ-Mn, the average magnetic moment decreases linearly from $2.4\mu_B$ according to the simple dilution line up to 30 at.% Fe. The calculated Fe LM is $1.65\mu_B$ in the impurity limit. It remains constant up to 20 at.% Fe and starts to decrease rapidly beyond 20 at.% Fe, while that of Mn is almost constant up to 30 at.% Fe.

The calculated average magnetic moment versus concentration curve explains the experimental curve up to 50 at.% Fe. The rigid-band calculation led to a similar concentration dependence up to 50 at.% Fe, but it failed to explain the minimum at 50 at.% Fe and the behaviour beyond 50 at.% Fe [9, 18]. The present result shows a minimum at 50 at.% Fe in agreement with the experimental data, and increases at 60 at.% Fe. The Fermi level there lies just at the peak of the nonmagnetic DOS. The enhancement of the average magnetic moment can be attributed to a large kinetic energy gain due to the change of the

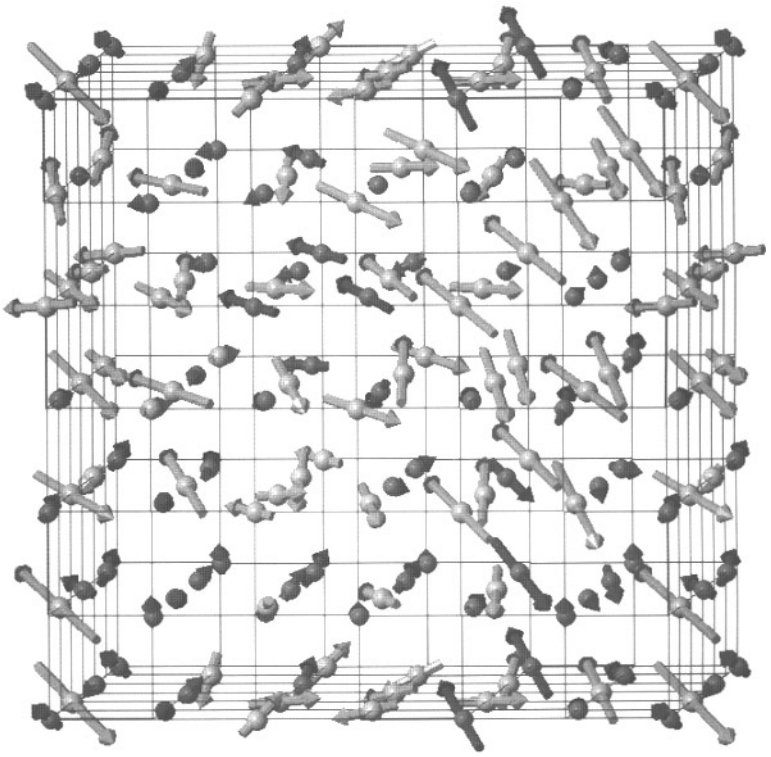

(d)

Figure 2. (Continued)

peak to a dip at the Fermi level upon polarization, as was mentioned in the last subsection. The average magnetic moment does not show a strong concentration dependence beyond 70 at.% Fe, although the Mn LMs start to increase beyond 80 at.% Fe with the localization of electrons at Mn sites due to decreasing transfer integrals.

The calculated average LMs in the concentration regions 0–30 at.% Fe and 90–100 at.% Fe are overestimated as compared with the experimental data. In both regions, the γ-FeMn alloys show tetragonal distortion. Recent ground-state calculations [30] show that the Fe LM changes sign in CsCl-type antiferromagnetic Mn, which is obtained by a 10% contraction of the c-axis in γ-Mn. Thus, there is a possibility that Fe LMs reduce in magnitude with tetragonal distortion. The effect of the tetragonal distortion will be discussed in a separate paper. Our results do not reproduce the large magnetic moment ($\sim 2.0\mu_B$) found from neutron experiments at around 70 at.% Fe. This might be attributed to the atomic short-range order or some local lattice distortion. These effects will be investigated in the future to resolve the disagreement between theory and experiments.

4. Summary

We have presented a MD approach to magnetic alloys with complex magnetic structures based on the isothermal MD method and the functional integral technique. The theory takes into account the configurational disorder in substitutional binary alloys by using random numbers. It reduces to the generalized Hartree–Fock approximation at the ground state,

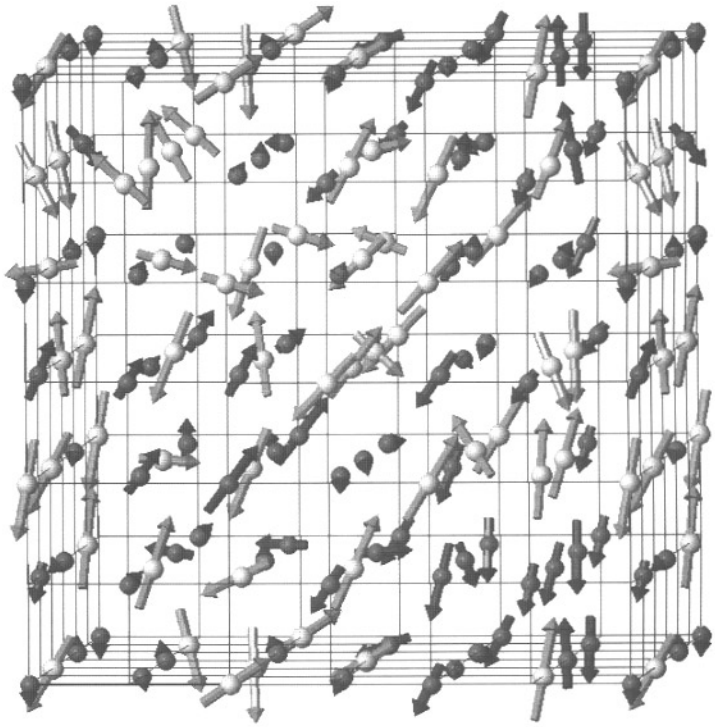

(e)

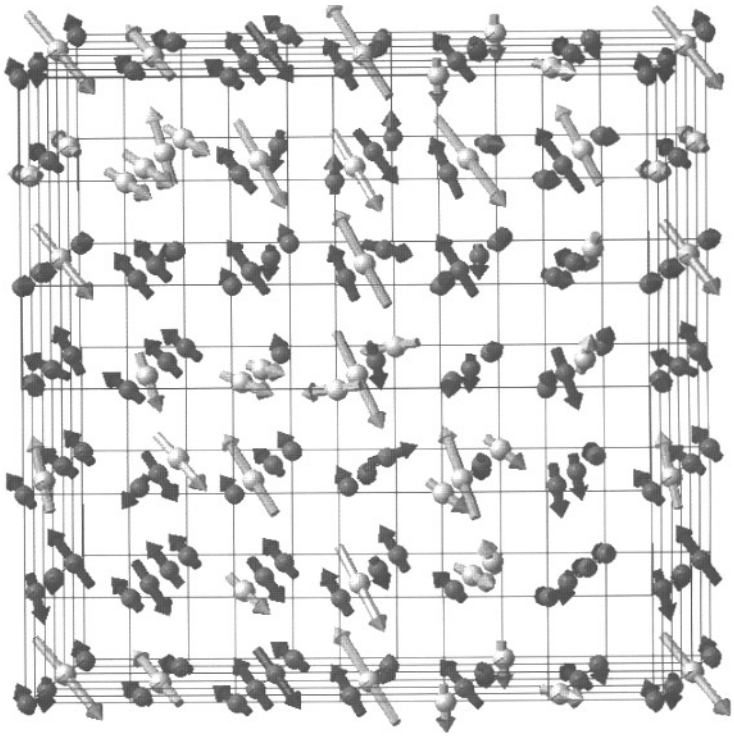

(f)

Figure 2. (Continued)

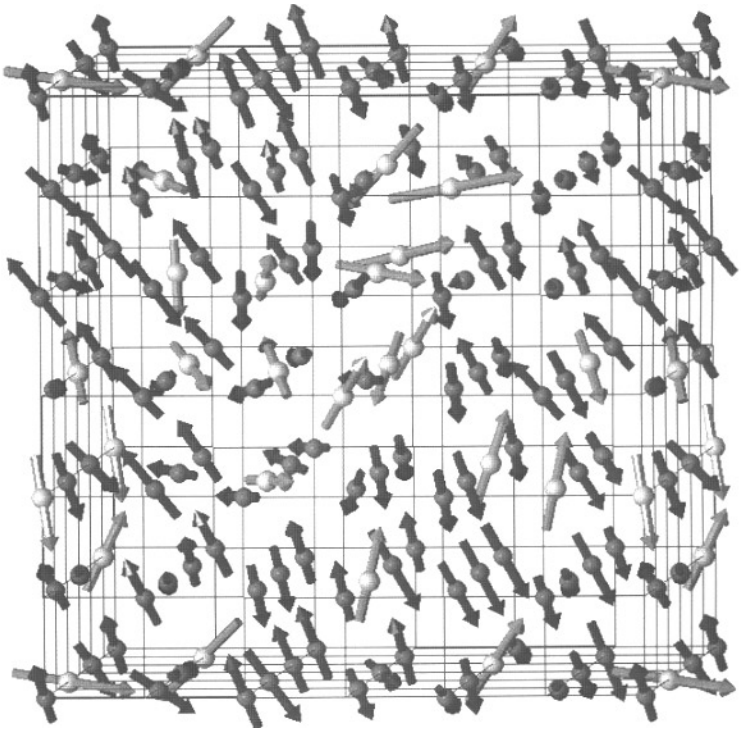

(g)

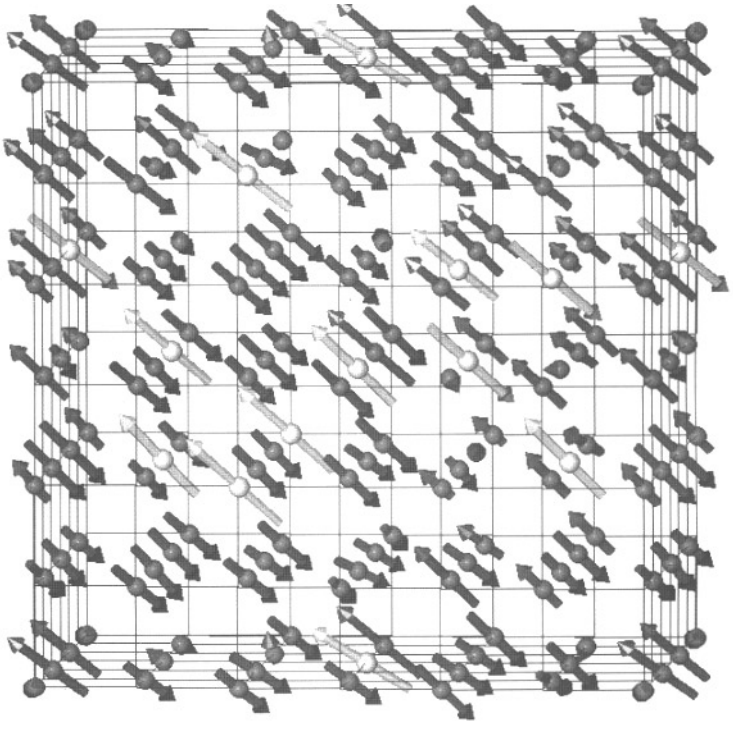

(h)

Figure 2. (Continued)

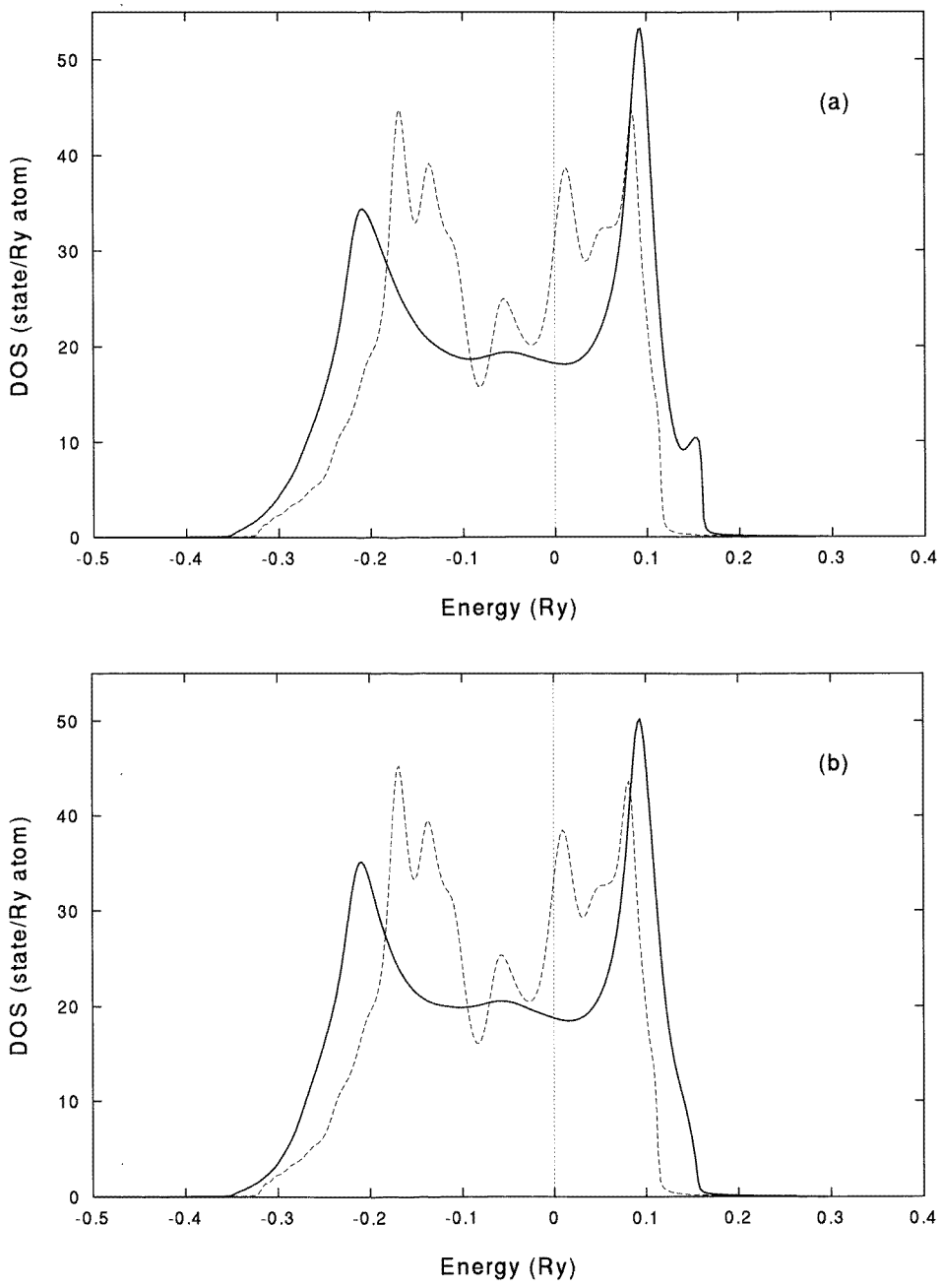

Figure 3. The total DOS at the ground state for various concentrations: (a) 10 at.% Fe; (b) 20 at.% Fe; (c) 50 at.% Fe; and (d) 60 at.% Fe. The dashed curves show the DOS in the nonmagnetic state. The vertical dotted lines indicate the Fermi level.

and describes the spin fluctuations at finite temperatures in a semi-classical way. The MD method assumes ergodicity for the motion of the fictitious LMs, and obtains the thermal average of the LMs by means of time averaging of the fictitious LMs after solving the

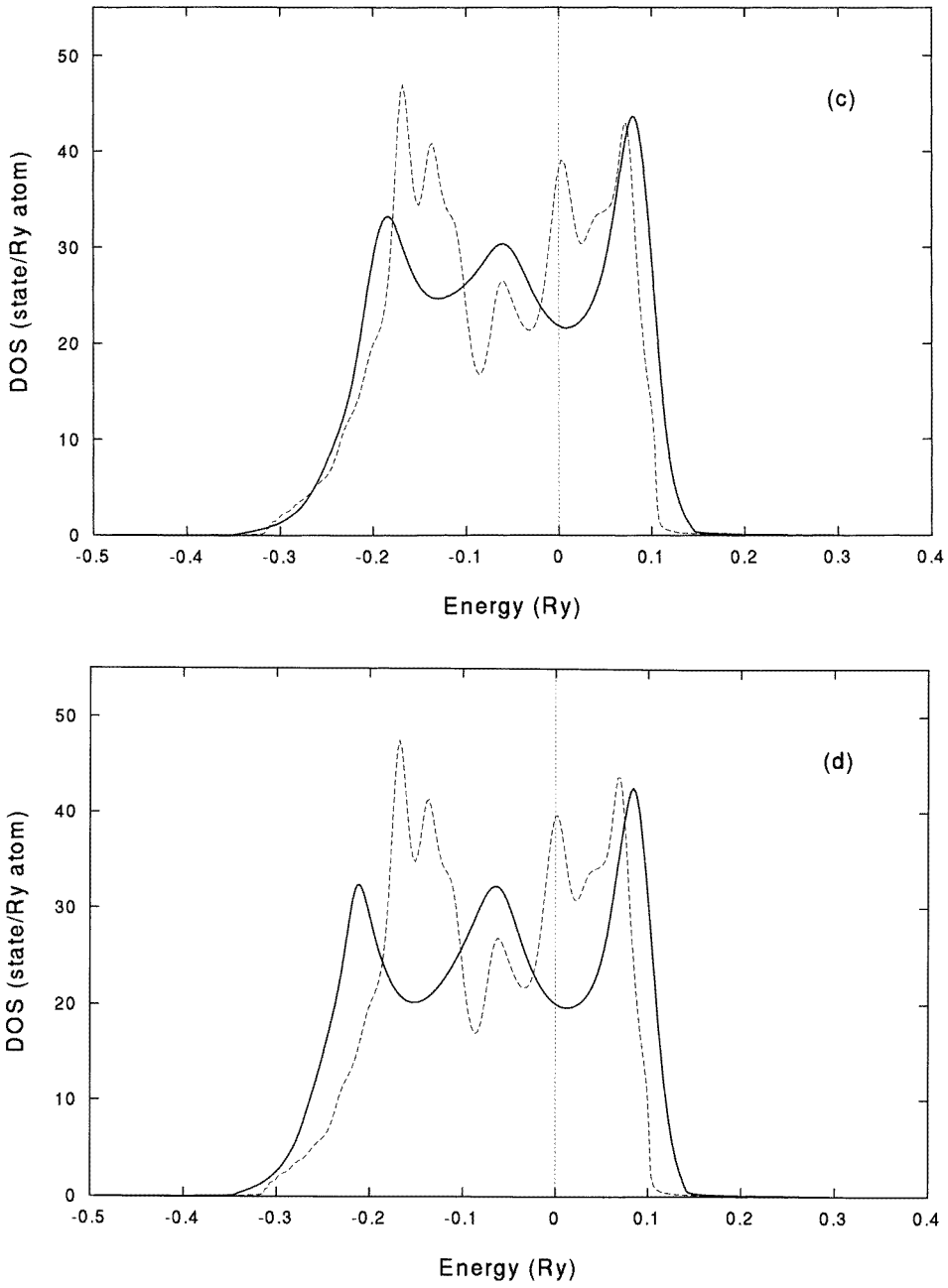

Figure 3. (Continued)

$6N+3$ equations of motion for the N fictitious LMs. The magnetic forces are calculated by using the recursion method at each MD step. The theory allows us to calculate automatically the magnetic structures of random magnetic alloys with a few hundred atoms in a unit cell at finite temperatures over all concentrations.

We performed the MD calculations using 108 atoms in a unit cell at 25 K to determine

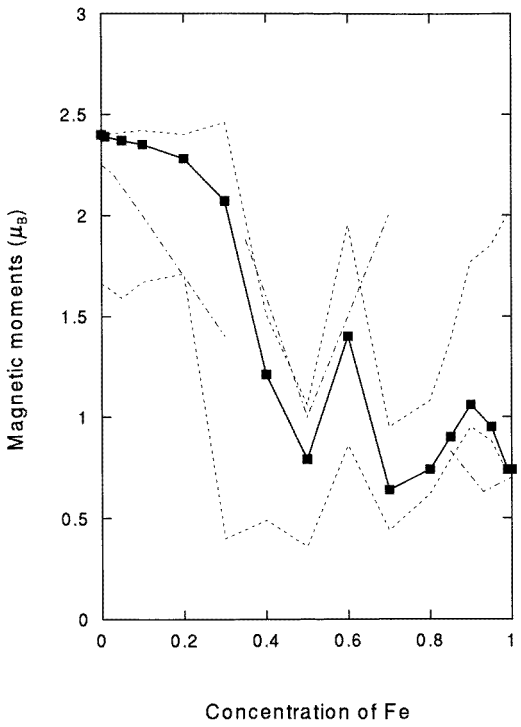

Figure 4. The concentration dependence of the magnetic moments in γ-FeMn alloys calculated by the MD method at 25 K. The solid line represents the average magnetic moments, and the upper (lower) dotted line represents the average Mn (Fe) magnetic moments. The chain lines represent the average magnetic moments obtained from the neutron experiments [14].

the magnetic structures as well as the magnetic moments of the disordered γ-FeMn alloys. It was demonstrated that the alloys form various complex magnetic structures due to competing interactions. The AFI structure was obtained up to 10 at.% Fe. Beyond 10 at.% Fe, the collinear structure changes to the various complex structures: the helix-like one at 20 at.% Fe, noncollinear structures between 30 and 60 at.% Fe, a collinear-like structure at 65 at.% Fe, noncollinear structures between 70 and 80 at.% Fe, collinear structures between 85 and 95 at.% Fe, and helical structures with $\boldsymbol{Q} = (0, 1/3, 2/3)\, 2\pi/a$ beyond 95 at.% Fe, which qualitatively explains the results obtained by the neutron diffraction experiments. The calculated DOSs for these magnetic structures are found to be consistent with the stabilities of the structures because of the existence of a dip near the Fermi energy.

The calculated magnetic moments explained the concentration dependence obtained from the neutron experiments. We found the existence of a peculiar minimum at 50 at.% Fe, which was not obtained by the rigid-band calculations. At 70 at.% Fe, we did not obtain the large magnetic moment ($\sim 2.0\mu_B$) found from the neutron experiment. The calculated average LMs for the concentration regions 0–30 at.% Fe and 90–100 at.% Fe are somewhat overestimated as compared with the experimental data, which was attributed to the tetragonal lattice distortion.

In our calculations, we used a rather small size of unit cell and adopted periodic boundary conditions to extend the system. Improved calculations could be done by considering a larger size of unit cell, which would reduce the problem caused by the periodic boundary

conditions. More detailed electronic structures should be taken into account in our MD calculations in the future with the use of a first-principles tight-binding LMTO (linear muffin-tin orbital) Hamiltonian to obtain more accurate magnetic structures.

Acknowledgment

This work was done partly using the facilities of the Supercomputer Centre, Institute for Solid State Physics, University of Tokyo.

References

[1] Moruzzi V L, Janak J F and Williams A R 1978 *Calculated Electronic Properties of Metals* (New York: Pergamon)
Moruzzi V L and Sommers B C 1995 *Calculated Electronic Properties of Ordered Alloys: A Handbook* (Singapore: World Scientific)
[2] Soven P 1968 *Phys. Rev.* **156** 809
Velický B, Kirkpatrick S and Ehrenreich H 1968 *Phys. Rev.* **175** 747
[3] Hasegawa H and Kanamori J 1971 *J. Phys. Soc. Japan* **31** 382
Hasegawa H and Kanamori J 1972 *J. Phys. Soc. Japan* **33** 1599
Hasegawa H and Kanamori J 1972 *J. Phys. Soc. Japan* **33** 1607
[4] Hubbard J 1979 *Phys. Rev.* B **19** 2626
Hubbard J 1979 *Phys. Rev.* B **20** 4584
Hubbard J 1981 *Phys. Rev.* B **23** 597
[5] Hasegawa H 1979 *J. Phys. Soc. Japan* **46** 1504
Hasegawa H 1980 *J. Phys. Soc. Japan* **49** 178
[6] Hasegawa H 1983 *J. Phys. F: Met. Phys.* **13** 1915
[7] Kakehashi Y 1986 *Phys. Rev.* B **34** 3243
[8] Kakehashi Y 1990 *Prog. Theor. Phys.* **101** 105
[9] Kakehashi Y, Akbar S and Kimura N J 1998 *Phys. Rev.* B at press
[10] Fulde P 1991 *Electron Correlations in Molecules and Solids (Springer Series in Solid State Sciences 100)* (Berlin: Springer)
[11] Nosé S 1984 *J. Chem. Phys.* **81** 511
[12] Hoover W G 1991 *Computational Statistical Mechanics* (Amsterdam: Elsevier)
[13] Tsunoda Y 1989 *J. Phys.: Condens. Matter* **1** 10 427
[14] Endoh Y and Ishikawa Y 1971 *J. Phys. Soc. Japan* **30** 1614
[15] Kennedy S J and Hicks T J 1986 *J. Phys. F: Met. Phys.* **17** 1599
[16] Bisanti P, Mazzone G and Sacchetti F 1987 *J. Phys. F: Met. Phys.* **17** 1425
[17] Andreani C, Mazzone G and Sacchetti F 1987 *J. Phys. F: Met. Phys.* **17** 1419
[18] Asano S and Yamashita J 1971 *J. Phys. Soc. Japan* **31** 1000
[19] Kübler J, Hock K H, Sticht J and Williams A R 1988 *J. Phys. F: Met. Phys.* **18** 469
[20] Fujii S, Ishida S and Asano S 1991 *J. Phys. Soc. Japan* **60** 4300
[21] Süss F and Krey U 1993 *J. Magn. Magn. Mater.* **125** 351
[22] Hubbard J 1959 *Phys. Rev. Lett.* **3** 77
[23] Stratonovich R L 1958 *Dokl. Akad. Nauk* **115** 1097 (Engl. Transl. 1958 *Sov. Phys.–Dokl.* **2** 416)
[24] Haydock R, Heine V and Kelly M J 1975 *J. Phys. C: Solid State Phys.* **8** 591
[25] Heine V, Haydock R and Kelly M J 1980 *Solid State Physics* vol 35 (New York: Academic) p 1
[26] Haydock R and Kelly M J 1973 *Surf. Sci.* **38** 139
[27] Andersen O K, Madsen J, Poulsen U K, Jepsen O and Kollär J 1977 *Physica* B **86–88** 249
[28] Janak J F 1977 *Phys. Rev.* B **16** 255
[29] Becon G E, Dunmur I W, Smith J H and Street R 1957 *Proc. R. Soc.* A **241** 223
[30] Antropov V P, Anisimov V I, Liechtenstein A I and Postnikov A V 1988 *Phys. Rev.* B **37** 5603